Elastic bending and active tilting of myosin heads during muscle contraction

eliminate emission from BFP. Conditions were the same as for the steady-state measurements apart from the protein concentration (1.0 μM).

Model building. We constructed structural models of GS1dCB in the M^{**}.ADP.P_i and M.ADP states using coordinates of the V_i and ADP structures of S1dC[11–13] and those of GFP[20]. As many residues of the C-terminal domain of S1dC are missing in the S1dC data, they were restored by fitting with the chicken S1 structure using the program Eos[25]. The myosin head with the lever-arm domain, assuming the V_i or ADP structure, was then reconstructed from the V_i or ADP structure of the *Dictyostelium* S1dC[11–13] and the structure of the lever-arm domain of chicken S1 (ref. 3) as before[5]. Next, we calculated the probability distribution of the position of fluorophore of BFP or GFP. The calculation was based on FRET data and the following assumptions: (1) the chain of GFP or BFP cannot occupy the same position as the S1dC chain; (2) the distance between the fluorophore of GFP and the N terminus of S1dC is 3.5 nm, and that between the fluorophore of BFP and the C terminus of S1dC is 2.5 nm, consistent with the atomic structure of GFP[20]; (3) each of the distances between the points (GFP fluorophore and N terminus of S1dC, GFP fluorophore and Cy3, BFP fluorophore and C terminus of S1dC, BFP fluorophore and Cy3, BFP fluorophore and GFP fluorophore) can vary around the measured value as though the points are connected by springs for which the spring constant is $k_BT/(0.25\,\mathrm{nm})^2$. By introducing this length variability, the error of the distance obtained by FRET measurements (the range of the standard deviation was 0.02–0.14 nm) and the error in the initial estimate of the position of Cy3 can be accommodated. Then we calculated the probability distribution of the fluorophore using two types of S1dC structure found in the PDB (Brookhaven Protein Data Bank) files under accession numbers 1mmd (S1dC complexed with MgADP.BeF_x) and 1vom (S1dC complexed with MgADP.V_i). The best probability distribution was obtained when we used the PDB files 1vom and 1mmd for the M^{**}.ADP.P_i and M.ADP states, respectively.

Received 27 May; accepted 10 September 1998.

1. Cooke, R. The mechanism of muscle contraction. *CRC Crit. Rev. Biochem.* **21,** 53–118 (1986).
2. Rayment, I. *et al.* Structure of the actin-myosin complex and its implications for muscle contraction. *Science* **261,** 58–65 (1993).
3. Rayment, I. *et al.* Three-dimensional structure of myosin subfragment-1: a molecular motor. *Science* **261,** 50–58 (1993).
4. Spudich, J. A. How molecular motors work. *Nature* **372,** 515–518 (1994).
5. Holmes, K. C. The swinging lever-arm hypothesis of muscle contraction. *Curr. Biol.* **7,** 112–118 (1997).
6. Prasher, D. C., Eckenrode, V. K., Ward, W. W., Prendergast, F. G. & Cormier, M. J. Primary structure of the *Aequorea victoria* green-fluorescent protein. *Gene* **111,** 229–233 (1992).
7. Heim, R. & Tsien, R. Y. Engineering green fluorescent protein for improved brightness, longer wavelengths and fluorescence resonance energy transfer. *Curr. Biol.* **6,** 178–182 (1996).
8. Miyawaki, A. *et al.* Fluorescent indicators for Ca2+ based on green fluorescent proteins and calmodulin. *Nature* **388,** 882–887 (1997).
9. Warrick, H. M., DeLozanne, A., Leinwand, L. A. & Spudich, J. A. Conserved protein domains in a myosin heavy chain gene from *Dictyostelium discoideum*. *Proc. Natl Acad. Sci. USA* **83,** 9433–9437 (1986).
10. Itakura, S. *et al.* Force-generating domain of myosin motor. *Biochem. Biophys. Res. Commun.* **196,** 1504–1510 (1993).
11. Gulick, A. M., Bauer, C. B., Thoden, J. B. & Rayment, I. X-ray structures of the MgADP, MgATPγS, and MgAMPPNP complexes of the *Dictyostelium discoideum* myosin motor domain. *Biochemistry* **36,** 11619–11628 (1997).
12. Smith, C. A. & Rayment, I. X-ray structure of te magnesium(II).ADP.vanadate complex of the *Dictyostelium discoideum* myosin motor domain to 1.2 Å resolution. *Biochemistry* **35,** 5404–5417 (1996).
13. Fisher, A. J. *et al.* X-ray structures of the myosin motor domain of *Dictyostelium discoideum* complexed with MgADP.BeF_x and MgADP.AlF_4. *Biochemistry* **34,** 8960–8972 (1995).
14. Lymn, R. W. & Taylor, E. W. Mechanism of adenosine triphosphate hydrolysis of actomyosin. *Biochemistry* **10,** 4617–4624 (1971).
15. Bagshaw, C. R. & Trentham, D. R. The characterization of myosin-product complexes and of product-release steps during the magnesium ion-dependent adenosine triphosphatase reaction. *Biochem. J.* **141,** 331–349 (1974).
16. Sasaki, N., Shimada, T. & Sutoh, K. Mutational analysis of the switch II loop of *Dictyostelium* myosin II. *J. Biol. Chem.* **273,** 20334–20340 (1998).
17. Kuhlman, P. A. & Bagshaw, C. R. ATPase kinetics of the *Dictyostelium discoideum* myosin II motor domain. *J. Muscle. Res. Cell. Motil.* **19,** 491–504 (1998).
18. Werber, M. M., Peyser, Y. M. & Muhlrad, A. Characterization of stable beryllium fluoride, aluminum fluoride, and vanadate containing myosin subfragment 1-nucleotide complexes. *Biochemistry* **31,** 7190–7197 (1992).
19. Maruta, S., Henry, G. D., Sykes, B. D. & Ikebe, M. Formation of the stable myosin–ADP–aluminum fluoride and myosin–ADP–beryllium fluoride complexes and their analysis using ^{19}F NMR. *J. Biol. Chem.* **268,** 7093–7100 (1993).
20. Ormo, M. *et al.* Crystal structure of the *Aequorea victoria* green fluorescent protein. *Science* **273,** 1392–1395 (1996).
21. Shimada, T., Sasaki, N., Ohkura, R. & Sutoh, K. Alanine scanning mutagenesis of the switch I region in the ATPase site of *Dictyostelium discoideum* myosin II. *Biochemistry* **36,** 14037–14043 (1997).
22. Clegg, R. M. Fluorescence resonance energy transfer and nucleic acids. *Methods Enzymol.* **211,** 353–388 (1992).
23. Stryer, L. Fluorescence energy transfer as a spectroscopic ruler. *Annu. Rev. Biochem.* **47,** 819–846 (1978).
24. Miki, M. Detection of conformational changes in actin by fluorescence resonance energy transfer between tyrosine-69 and cysteine-374. *Biochemistry* **30,** 10878–10884 (1991).
25. Yasunaga, T. & Wakabayashi, T. Extensible and object-oriented system Eos supplies a new environment for image analysis of electron micrographs of macromolecules. *J. Struct. Biol.* **116,** 155–160 (1996).
26. Jones, T. A., Zou, J. Y., Cowan, S. W. & Kjeldgaard, M. Improved methods for building protein models in electron density maps and the location of errors in these models. *Acta Crystallogr. A* **47,** 110–119 (1991).

Acknowledgements. We thank K. Oiwa for Cy3 nucleotides, M. Miki for discussions about the FRET experiments, and M. Steward, C. Bagshaw and P. Kuhlman for critically reading the manuscript.

Correspondence and requests for materials should be addressed to K.S. (e-mail: cksutoh@komaba.ecc.u-tokyo.ac.jp).

Elastic bending and active tilting of myosin heads during muscle contraction

Ian Dobbie*, Marco Linari†, Gabriella Piazzesi†, Massimo Reconditi†, Natalia Koubassova‡, Michael A. Ferenczi§, Vincenzo Lombardi† & Malcolm Irving*

** Randall Institute, King's College London, London WC2B 5RL, UK*
† Dipartimento di Scienze Fisiologiche, Università degli Studi di Firenze, Viale GB Morgagni 63, I-50134 Firenze, Italy
‡ Institute of Mechanics, Moscow State University, Moscow 119899, Russia
§ National Institute for Medical Research, Mill Hill, London NW7 1AA, UK

Muscle contraction is driven by a change in shape of the myosin head region that links the actin and myosin filaments[1,2]. Tilting of the light-chain domain of the head with respect to its actin-bound catalytic domain is thought to be coupled to the ATPase cycle[3–6]. Here, using X-ray diffraction and mechanical data from isolated muscle fibres, we characterize an elastic bending of the heads that is independent of the presence of ATP. Together, the tilting and bending motions can explain force generation in isometric muscle, when filament sliding is prevented. The elastic strain in the head is 2.0–2.7 nm under these conditions, contributing 40–50% of the compliance of the muscle sarcomere. We present an atomic model for changes in head conformation that accurately reproduces the changes in the X-ray diffraction pattern seen when rapid length changes are applied to muscle fibres both in active contraction and in the absence of ATP. The model predictions are relatively independent of which parts of the head are assumed to bend or tilt, but depend critically on the measured values of filament sliding and elastic strain.

We measured the elastic properties of the actin and myosin filaments and myosin heads in actively contracting single muscle fibres by imposing a sinusoidal length change of about 5 nm per half-sarcomere, peak-to-peak with period 320 μs (Fig. 1). The force oscillated between about 0.6 and 1.6 T_0, where T_0 is the steady force during isometric contraction (Fig. 1a). No phase difference could be detected between the force and sarcomere length changes with the 8-μs sampling interval (Fig. 1b). Thus the length changes are sufficiently fast, and the compliance of the fibre attachments sufficiently small, that the force response is purely elastic[7]; neither the rapid force recovery associated with the working stroke in the attached myosin head[8], nor the slower detachment of myosin heads from actin and reattachment to it[9,10] contribute to the force response during the 320-μs cycle.

Elastic deformation of myosin heads alters the intensity of the M3 X-ray reflection (I_{M3}) arising from the 14.5-nm spacing between adjacent sets of myosin heads along the filaments[11,12]. I_{M3} decreased by 25 ± 3% (mean ± s.e., 5 fibres) during the stretch phase of the length-change cycle (Fig. 1c, filled circles). The change in I_{M3}, recorded at 20-μs time resolution, was exactly 180° out of phase

with the length and force signals. Thus the motion of the myosin heads in this protocol is purely elastic, like the mechanical response.

The compliance of the myosin filaments was estimated from the spacing of the M3 reflection, and that of the actin filaments from the spacing of the 5.9-nm layer line reflection from the actin helix, by comparing 100-μs time-frames at the peak and trough of the force oscillation. The strains in the myosin and actin filaments were $0.12 \pm 0.01\%/T_0$ and $0.30 \pm 0.13\%/T_0$ respectively (±s.e., 5 fibres), in agreement with the spacing changes of a wider range of X-ray reflections during slow stretch of whole muscles[13,14]. Our results show that these spacing changes are not caused by attachment or detachment of the myosin heads or by the working stroke in the attached heads, processes that are slower than the length-change cycle used here.

The total compliance of the muscle fibre segment illuminated by the X-ray beam during the 320-μs length-change cycle was 5.1 (± 0.3) nm/T_0 in each half-sarcomere. This includes the contributions of myosin and actin filaments and the myosin heads that crosslink them in the zone of filament overlap. The contributions of the myosin and actin filaments were calculated from the X-ray measurements of average filament strain, taking into account the strain distribution along the filaments[15,16], as 0.8 and 2.3 nm/T_0 respectively. Neglecting possible small contributions from other sarcomeric structures, the remaining 2.0 nm/T_0 of the half-sarcomere compliance in active contraction should be due to the myosin heads. The main source of uncertainty in this estimate is our value of $0.30 \pm 0.13\%/T_0$ for the average strain in the actin filament. If this were replaced by the more precise published values, either $0.23 \pm 0.01\%/T_0$ from the spacing change of the 2.7 nm actin-based X-ray reflection during slow stretch of whole muscles[13], or $0.21 \pm 0.03\%/T_0$ from the variation of sarcomere compliance with sarcomere length in isolated fibres[16], the myosin head compliance would be about 2.7 nm/T_0.

Elastic deformation of myosin heads should still be present in the absence of ATP (in rigor), when all the myosin heads are bound to actin[17,18]. To test this prediction, we applied a peak-to-peak length change of 2.4 nm per half-sarcomere and period of 320 μs to fibres that had been permeabilized and depleted of ATP (Fig. 2). The

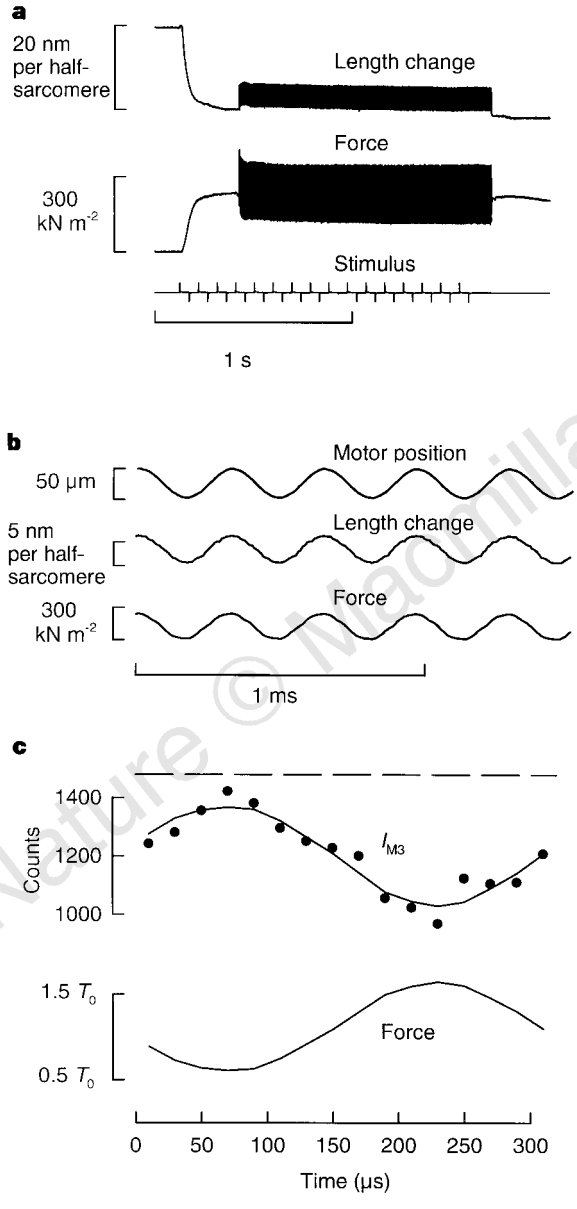

Figure 1 Changes in force and intensity of the M3 X-ray reflection (I_{M3}) produced by rapid length oscillations. **a**, Length change (nm per half-sarcomere) of the segment in the X-ray beam and force, when 4,000 oscillations with period of 320 μs were imposed during electrical stimulation of an intact muscle fibre; cross-sectional area, 20,100 μm^2; length, 6.63 mm; mean sarcomere length in the 2.34 mm segment, 2.09 μm. **b**, Changes in motor position, segment length and force, sampled at 8-μs intervals 1 s after the start of the oscillations. **c**, I_{M3} (filled circles) and force (continuous lines; that in the upper panel inverted and scaled to fit I_{M3}) averaged over the 4,000 cycles from 61 tetani in 5 fibres; peak-to-peak length change 5.27 ± 0.12 nm per half-sarcomere. Dashed line: I_{M3} without applied length changes in the same fibres (11 tetani).

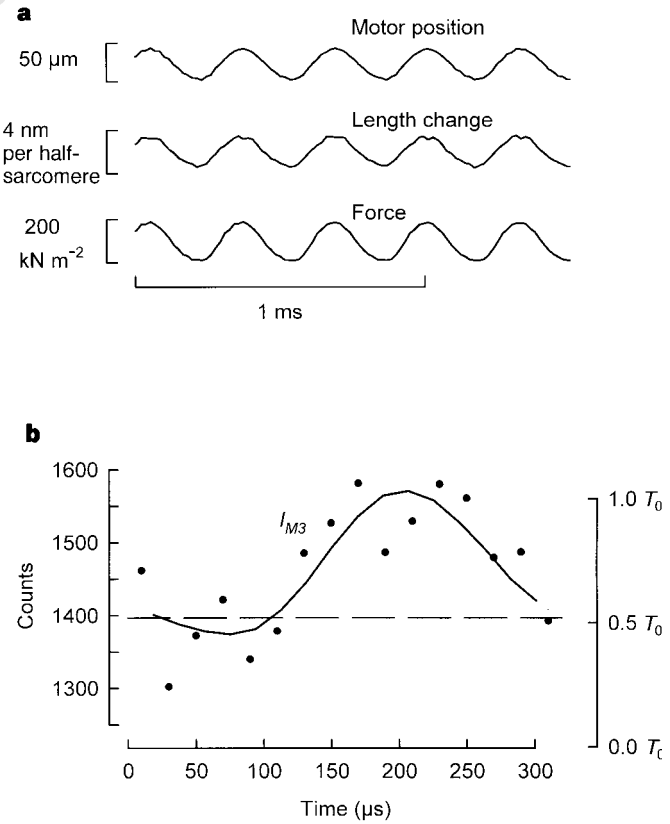

Figure 2 Changes in force and I_{M3} produced by length oscillations with 320 μs period in rigor. **a**, Motor position, length change of segment in the X-ray beam, and force sampled at 16-μs intervals starting 30 ms after the start of 4,000 stretch-shortening cycles. Before the oscillations force was 0.51 T_0; fibre length, 3.52 mm; mean sarcomere length in the 2.16 mm segment, 2.15 μm. Cross-sectional area: 21,100 μm^2 in the intact fibre, 24,800 μm^2 in rigor. **b**, I_{M3} (filled circles) and force, summed over the 4,000 cycles, from 200 runs in 8 fibres, peak-to-peak length change, 2.4 ± 0.1 nm per half-sarcomere. Dashed line: I_{M3} without imposed length changes in the same fibres (29 runs); force was similar to the minimum value during oscillations.

resulting force modulation was $0.57 \pm 0.02\,T_0$ (±s.e., 8 fibres), corresponding to a half-sarcomere compliance of $4.3 \pm 0.2\,\mathrm{nm}/T_0$. There was no detectable phase lag between the sarcomere length and force signals (Fig. 2a), as expected for a purely elastic response. I_{M3} increased by 14 ± 4% during the stretch (Fig. 2b); this change is in the opposite direction to that seen in active contraction (Fig. 1c), as reported previously for slower length changes[19]. The spacings of the X-ray reflections could not be measured precisely in rigor but, assuming that filament compliances have the same value as in active contraction[20], the compliance of the myosin heads in rigor would be $1.2\,\mathrm{nm}/T_0$, or about $1.9\,\mathrm{nm}/T_0$ if we use published values of actin filament compliance[13,16] as above.

We constructed an atomic model for the compliance of the myosin head based on elastic bending of its light-chain domain (Fig. 3). Head conformation in an unstrained rigor fibre (Fig. 3a) was assumed to be the same as that deduced from electron micrographs of isolated actin filaments decorated with myosin head fragments[3]. When a fibre in rigor is stretched, the light-chain domain of the head is displaced towards the M line of the sarcomere (upwards in Fig. 3b), so the axial position of its centre of mass moves closer to that of the catalytic domain. The mass projection of the head onto the filament axis becomes narrower, so I_{M3} increases, as we observed. The size of the increase depends on the myosin head compliance; the observed increase of 14 ± 4% (Fig. 2b) requires a head compliance of $1.3 \pm 0.4\,\mathrm{nm}/T_0$, in agreement with the value of $1.2–1.9\,\mathrm{nm}/T_0$ in rigor estimated above.

In active contraction, I_{M3} decreases during a stretch (Fig. 1c). This can only be explained by bending of the light-chain domain if it has already tilted substantially away from the rigor conformation during active contraction. Following current models for the changes in myosin head conformation during the ATPase cycle[3–6], we represented this active motion as tilting of the entire light-chain domain with respect to the actin-bound catalytic domain. Starting from the unstrained rigor conformation, the light-chain domain must be tilted by 22° towards the M line of the half-sarcomere to give the narrowest projection of the mass of the whole head on the filament axis, and thus the maximum value of I_{M3}. Experimentally, I_{M3} is maximized by shortening of ~1 nm per half-sarcomere from the active isometric conformation[21], which corresponds to tilting the light-chain domain away from the M line by ~8°. Thus the total tilt between rigor and active isometric contraction is about 30°.

In the experiment shown in Fig. 1, the average force is higher than in isometric contraction and I_{M3} is lower (Fig. 1a, c). This suggests that the light-chain domain is tilted upwards by a further ~10° from its isometric conformation during this protocol (Fig. 3c). When an active fibre is stretched, bending of the light-chain domain displaces its centre of mass away from that of the catalytic domain, so I_{M3} decreases, as we observe. The decrease of 25 ± 3% in the experiment shown in Fig. 1 requires a myosin head compliance in active contraction of $2.3 \pm 0.3\,\mathrm{nm}/T_0$, in agreement with the value $2.0–2.7\,\mathrm{nm}/T_0$ estimated above from the filament and sarcomere compliances.

According to this model, the tilting motion associated with the ATPase cycle can still occur during isometric contraction, when filament sliding is prevented and the strain in the filaments is constant. In these conditions, the local conformational change at the junction between the catalytic and light-chain domains is accommodated by elastic bending of the light-chain domain, so that the head–rod junction does not move with respect to the actin-binding site. The resulting change in head conformation would be difficult to detect by low-resolution structural methods.

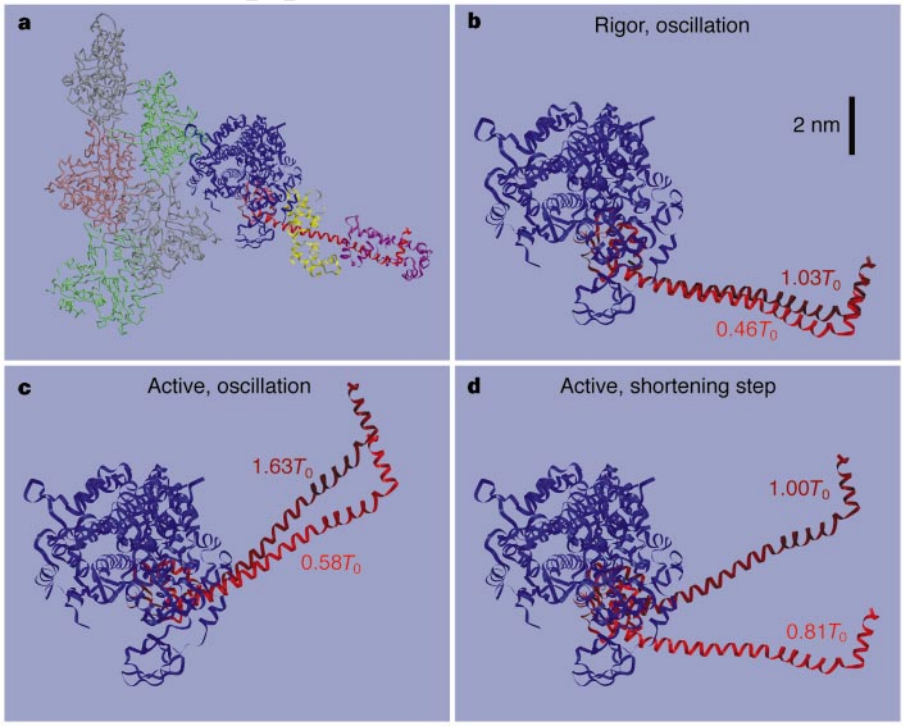

Figure 3 Structural model for elastic bending and ATP-driven tilting of the light-chain domain of the myosin head. **a**, Catalytic (heavy-chain residues 1–707, blue; 707–770, pink) and light-chain domains (heavy-chain residues 771–843, red; essential light chain, yellow; regulatory light chain, magenta) of the myosin head, bound to a vertical actin filament (grey, green, brown) in rigor, with the sarcomeric M line at the top of the figure. In **b**–**d**, to which the scale bar in **b** applies, actin and light chains are omitted for clarity, catalytic domain (blue) is in the same conformation as **a**, and the moving part of heavy chain (residues 707–843) is shown in red. **b**, Elastic bending of light-chain domain in rigor (Fig. 2), between force $0.46\,T_0$ (light red) and $1.03\,T_0$ (dark red). **c**, Elastic bending of light-chain domain during active contraction (Fig. 1) between $0.58\,T_0$ (light red) and $1.63\,T_0$ (dark red). **d**, Head conformation before (force, $1.00\,T_0$, dark red) and 2 ms after (force, $0.81\,T_0$; light red) a shortening step of 5.6 nm per half-sarcomere during active contraction. The conformations shown were calculated assuming a myosin head compliance of $1.2\,\mathrm{nm}/T_0$ in rigor and $2.0\,\mathrm{nm}/T_0$ in active contraction. The tilt angle between the light-chain and catalytic domains, relative to that in rigor, was 40° in **c**, 30° at $1.00\,T_0$ and 0° at $0.81\,T_0$ in **d**. Graphics prepared using Raster3D[30]. Coordinates kindly provided by I. Rayment[3].

Much larger changes in head conformation would occur if filament sliding were allowed. When a rapid shortening step is imposed during active contraction, I_{M3} decreases during the rapid force recovery that follows the step[12,22], and we suggested previously that this elementary force-generating process is due to a change in conformation of the myosin heads. When a shortening step of 5.6 nm per half-sarcomere is imposed from the isometric force level (T_0), force recovers to 0.81 T_0 by 2 ms after the step[12], so the change in elastic strain is only 1.0 nm and the remaining 4.6 nm must be accounted for by tilting of the light-chain domain (Fig. 3d). The required tilt angle is 30°, which brings the head to its rigor conformation. Moreover, the observed decrease in I_{M3}, 29 ± 6% (mean ± s.e., $n = 7$; see Fig. 4 of ref. 12), gives an independent estimate of the required tilt angle, 28.5 ± 2.5°, which is in good agreement with that calculated from the filament displacement.

This structural model for the function of the myosin motor has only two parameters: the tilt of the light-chain domain and the elastic strain. The changes in these two parameters can be calculated from measurements of the filament displacement, the force change, and the compliances of the myosin head and sarcomere. The observed changes in I_{M3} were consistent with the predictions of this structural model in a wide range of conditions (our Figs 1 and 2, and Fig. 4 of ref. 12). I_{M3} is relatively insensitive to the assumptions about which parts of the head bend or tilt. For example, a localized elastic element at the junction between the catalytic and light-chain domains would have an effect very similar to that of uniform bending of the light-chain domain. Further, tilting of the whole head around its actin-binding site would produce a decrease in I_{M3} in the protocol in Fig. 3d, similar to that produced by tilting at the catalytic/light-chain domain boundary, for the same amount of filament sliding. The critical features of the model for reproducing the observed changes in I_{M3} are the value of the myosin head compliance and the overall tilt of the heads towards the M line during isometric contraction.

The elastic deformation described here for myosin is likely to be a fundamental property of motor proteins, including those of the kinesin and dynein families. All these motors are thought to work by an ATP-driven change in conformation of a domain analogous to the myosin head. Many of them have a region analogous to the myosin light-chain domain which could amplify small conformational changes around the ATP-binding site into nanometre-scale movements. Motor compliance may be an unavoidable consequence of this lever-arm design[23], but the compliance itself has important functional advantages. It allows force generation against an immobile cargo. It provides a sensor for modulation of the ATPase activity by the external load, as required for efficient energy transduction. Finally, as most motor proteins have more than one head domain attached to a single tail, compliance within the head allows two or more heads to work together. □

Methods

Fibre mechanics. Mechanical measurements on single fibres from anterior tibialis muscles of *Rana temporaria* were made at 3–4 °C as described[16,24]. Average sarcomere length in the ~2 mm segment in the X-ray beam was measured by a striation follower. Intact fibres were electrically stimulated for 1.5 s; after 0.3 s at constant length, 4,000 stretch-shortening cycles were applied (Fig. 1a); after the first 10 ms of imposed length oscillation the force response was the same in each cycle, whether the oscillation began with a stretch or release[10,25]. For rigor experiments (Fig. 2), isolated fibres were permeabilized in relaxing solution (5.4 mM Na_2ATP, 7.7 mM $MgCl_2$, 25 mM EGTA, 19.1 mM creatine phosphate, 1 mg ml^{-1} creatine kinase, 20 mM butanedione monoxime (BDM), 100 mM TES, 10 mM reduced glutathione) containing α-toxin at 18 °C for 20 min[16,26]. Rigor was induced at zero force by incubating in rigor solution (34 mM EDTA, 100 mM TES) plus 20 mM BDM, for 10 min at 0 °C[20,27]. Fibres were stretched by ~4 nm per half-sarcomere at constant velocity for 1.5 s, 4,000 stretch-shortening cycles were imposed, then fibre length was slowly returned to its initial value.

X-ray diffraction. X-ray diffraction measurements were made at stations 2.1 and 16.1 of the CLRC Daresbury Laboratory, UK, with a monochromator/mirror X-ray camera and two-dimensional gas-filled detector[28]. Fibre-to-detector distance was 2.3 or 3.1 m. X-ray data were analysed using the XOTOKO and BSL packages from Daresbury. Reflection intensities were measured after fitting and subtracting a linear background; the intensity of the M3 reflection (I_{M3}), which has a spacing of about 14.5 nm in active contraction and rigor, was calculated by integrating between reciprocal spacings of 1/12.5 and 1/17.6 nm^{-1} axially and 1/91 nm^{-1} on either side of the meridian in active intact fibres (Fig. 1) and 1/13.1, 1/15.9 nm^{-1} and 1/130 nm^{-1}, respectively, in rigor (Fig. 2). There was no significant change in the width of the M3 reflection during the length-change cycle either along or across the meridian, in either condition. For precise measurements of reflection spacings, a polynomial background was subtracted and the centre of each reflection determined either by fitting a gaussian (Peakfit, Jandel Scientific) or from the centre-of-mass calculated with the program HV written by A. Stewart. The spacing of the 5.9-nm actin-based layer line was measured by integrating from 1/91 to 1/6.5 nm^{-1} from the meridian; its intensity changed by only 5% during the length-change cycle, increasing during the stretch.

Structural model. The effects of myosin head deformation on I_{M3} were calculated for bending of the light-chain domain (Fig. 3) as a uniform rod clamped at residue 770 under an axial strain (z) at residue 843. Axial displacement of each atom, assumed to be parallel to the 829–843 vector, was calculated as $z^*(3L - x)x^2/2L^3$, where x is distance of the atom from residue 770 and L is the value of x at residue 829, the sharp bend in the long heavy-chain helix. Residues between 829 and 843 were assigned $x = L$. ATP-driven tilting of the light-chain domain was at residue 707.

I_{M3} was initially calculated from the 1/14.5 nm^{-1} Fourier component of the axial mass projection of the myosin head, including every atom of both the heavy and light chains, assuming that the population of myosin heads that respond to a length step and bear the active force all have the same conformation and are responsible for the observed changes in I_{M3} (ref. 29). The calculations were repeated with different values for myosin head compliance in order to find the compliance required to reproduce the observed changes in I_{M3}. The single-conformation model is unrealistic in that the catalytic domains of myosin heads with head/rod junctions on a 14.5 nm axial repeat could not bind to actin sites with a 5.5 nm axial repeat. We calculated the effects of the mismatch in filament periodicities for an array of 50 myosin heads with their head-rod junctions (residue 843) fixed on a 14.5 nm repeat. In addition to the elastic strain and inter-domain tilt parameters used in the single-conformation model, the extra strain required for the catalytic domain to bind in its normal conformation to the nearest actin site was simulated by applying an additional strain, chosen at random in the range ±2.75 nm, to the light-chain domain of each individual head. The Fourier transform in the region of 1/14.5 nm^{-1} was then calculated for the axial mass projection of the 50-head array. The static values of I_{M3} were reduced by about one third compared to those from the single-conformation model, but the fractional changes in I_{M3} produced by the length-change protocols in Fig. 3b–d were essentially the same as in the single-conformation model. The latter gives an accurate estimate of fractional changes in I_{M3} for the protocols used here because the effect of conformational dispersion is constant during the synchronous conformational change produced by rapid length changes, as shown analytically for the case of three populations of heads with different conformations[22].

Received 9 February; accepted 18 September 1998.

1. Huxley, H. E. The mechanism of muscular contraction. *Science* **164,** 1356–1366 (1969).
2. Huxley, A. F. Muscular contraction. *J. Physiol. (Lond.)* **243,** 1–43 (1974).
3. Rayment, I. *et al.* Structure of the actin–myosin complex and its implications for muscle contraction. *Science* **261,** 58–65 (1993).
4. Rayment, I. *et al.* Three-dimensional structure of myosin subfragment-1: a molecular motor. *Science* **261,** 50–58 (1993).
5. Irving, M. *et al.* Tilting of the light chain region of myosin during step length changes and active force generation in skeletal muscle. *Nature* **375,** 688–691 (1995).
6. Cooke, R. Actomyosin interaction in striated muscle. *Physiol. Rev.* **77,** 671–697 (1997).
7. Cecchi, G., Griffiths, P. J. & Taylor, S. Muscular contraction: kinetics of cross-bridge attachment studied by high-frequency stiffness measurements. *Science* **217,** 70–72 (1982).
8. Huxley, A. F. & Simmons, R. M. Proposed mechanism of force generation in striated muscle. *Nature* **233,** 533–538 (1971).
9. Huxley, A. F. Muscle structure and theories of contraction. *Prog. Biophys. Biophys. Chem.* **7,** 255–318 (1957).
10. Lombardi, V., Piazzesi, G. & Linari, M. Rapid regeneration of the actin-myosin power stroke in contracting muscle. *Nature* **355,** 638–641 (1992).

11. Huxley, H. E., Faruqi, A. R., Kress, M., Bordas, J. & Koch, M. H. J. Time resolved X-ray diffraction studies of the myosin layer line reflections during muscle contraction. *J. Mol. Biol.* **158,** 637–684 (1982).
12. Lombardi, V. *et al.* Elastic distortion of myosin heads and repriming of the working stroke in muscle. *Nature* **374,** 553–555 (1995).
13. Huxley, H. E., Stewart, A., Sosa, H. & Irving, T. X-ray diffraction measurements of the extensibility of actin and myosin filaments in contracting muscle. *Biophys. J.* **67,** 2411–2421 (1994).
14. Wakabayashi, K. *et al.* X-ray diffraction evidence for the extensibility of actin and myosin filaments during muscle contraction. *Biophys. J.* **67,** 2422–2435 (1994).
15. Ford, L. E., Huxley, A. F. & Simmons, R. M. The relation between stiffness and filament overlap in stimulated frog muscle fibres. *J. Physiol. (Lond.)* **311,** 219–249 (1981).
16. Linari, M. *et al.* The stiffness of skeletal muscle in isometric contraction and rigor: the fraction of myosin heads bound to actin. *Biophys. J.* **74,** 2459–2473 (1998).
17. Cooke, R. & Franks, K. All myosin heads form bonds with actin in rigor rabbit skeletal muscle. *Biochemistry* **19,** 2265–2269 (1980).
18. Lovell, S. J., Knight, P. J. & Harrington, W. F. Fraction of myosin heads bound to thin filaments in rigor fibrils from insect flight and vertebrate muscles. *Nature* **293,** 664–666 (1981).
19. Yagi, N. *et al.* Small-angle X-ray diffraction of muscle using undulator radiation from the Tristan main ring at KEK. *J. Synchrotron Rad.* **3,** 305–312 (1996).
20. Higuchi, H., Yanagida, T. & Goldman, Y. E. Compliance of thin filaments in skinned fibers of rabbit skeletal muscle. *Biophys. J.* **69,** 1000–1010 (1995).
21. Piazzesi, G. *et al.* Changes in the X-ray diffraction pattern from single intact muscle fibres produced by rapid shortening and stretch. *Biophys. J.* **68** (suppl.), 92–96 (1995).
22. Irving, M., Lombardi, V., Piazzesi, G. & Ferenczi, M. A. Myosin head movements are synchronous with the elementary force-generating process in muscle. *Nature* **357,** 156–158 (1992).
23. Howard, J. & Spudich, J. A. Is the lever arm of myosin a molecular elastic element? *Proc. Natl Acad. Sci.* **93,** 4462–4464 (1996).
24. Lombardi, V. & Piazzesi, G. The contractile response during steady lengthening of stimulated frog muscle fibres. *J. Physiol. (Lond.)* **431,** 141–171 (1990).
25. Piazzesi, G., Linari, M., Reconditi, M., Vanzi, F. & Lombardi, V. Cross-bridge detachment and attachment following a step stretch imposed on active single frog muscle fibres. *J. Physiol. (Lond.)* **498,** 3–15 (1997).
26. Nishiye, E., Somlyo, A. V., Török, K. & Somlyo, A. P. The effect of MgADP on crossbridge kinetics: a laser flash photolysis study of guinea pig smooth muscle. *J. Physiol. (Lond.)* **460,** 247–271 (1993).
27. Bershitsky, S. *et al.* Mechanical and structural properties underlying contraction of skeletal muscle fibers after partial EDC cross-linking. *Biophys. J.* **71,** 1462–1474 (1996).
28. Towns-Andrews, E. *et al.* Time-resolved X-ray diffraction station: X-ray optics, detectors, and data acquisition. *Rev. Sci. Instrum.* **60,** 2346–2349 (1989).
29. Irving, M. & Piazzesi, G. Motions of myosin heads that drive muscle contraction. *News Physiol. Sci.* **12,** 249–254 (1997).
30. Merritt, E. A. & Bacon, D. J. Raster3D: Photorealistic molecular graphics. *Methods Enzymol.* **277,** 505–524 (1997).

Acknowledgements. We thank the non-crystalline diffraction and detector development teams at the CLRC Daresbury Laboratory for hardware and software for the X-ray measurements, A. Aiazzi and M. Dolfi for skilled mechanical and electronic assistance, and the UK MRC, EC, Intas, CNR (Italy), and Telethon (Italy) for financial support.

Correspondence should be addressed to M.I.

New pathway to polyketides in plants

Stefan Eckermann*, Gudrun Schröder*, Jürgen Schmidt†, Dieter Strack†, Ru A. Edrada‡, Yrjö Helariutta§‖, Paula Elomaa§, Mika Kotilainen§, Ilkka Kilpeläinen§, Peter Proksch‡, Teemu H. Teeri§ & Joachim Schröder*

** Institut für Biologie II, Universität Freiburg, Schänzlestrasse 1, 79104 Freiburg, Germany*
† Institut für Pflanzenbiochemie, Weinberg 3, 06120 Halle (Saale), Germany
‡ Lehrstuhl für Pharmazeutische Biologie, Mittlerer Dallenbergweg 64, 97082 Würzburg, Germany
§ Institute of Biotechnology, Viikki Biocenter, PO Box 56, FIN-00014 University of Helsinki, Finland

The repertoire of secondary metabolism (involving the production of compounds not essential for growth) in the plant kingdom is enormous, but the genetic and functional basis for this diversity is hard to analyse as many of the biosynthetic enzymes are unknown. We have now identified a key enzyme in the ornamental plant *Gerbera hybrida* (Asteraceae) that participates in the biosynthesis of compounds that contribute to insect and pathogen resistance. Plants transformed with an antisense construct of *gchs2*, a complementary DNA encoding a previously unknown function[1,2], completely lack the pyrone derivatives gerberin and parasorboside. The recombinant plant protein catalyses the principal reaction in the biosynthesis of these derivatives: GCHS2 is a polyketide synthase that uses acetyl-CoA and two condensation reactions with malonyl-CoA to form the pyrone backbone of the natural products. The enzyme also accepts benzoyl-CoA to synthesize the backbone of substances that have become of interest as inhibitors of the HIV-1 protease[3–5]. GCHS2 is related to chalcone synthase (CHS) and its properties define a new class of function in the protein superfamily. It appears that CHS-related enzymes are involved in the biosynthesis of a much larger range of plant products than was previously realized.

CHS, stilbene synthase and acridone synthase are polyketide synthases that are found in plants; they share >65% identity. They use aromatic CoA-esters as a starter substrate, perform three condensation reactions with malonyl-CoA, and form new aromatic ring systems[6]. We have previously characterized cDNAs encoding two CHS enzymes from *G. hybrida* and a cDNA encoding a CHS-like protein (GCHS2) with 73% identity to the CHS enzymes. In contrast to CHS, GCHS2 is highly expressed in almost all tissues of the plant. Its presence does not correlate with flavonoid biosynthesis[1], and its substrate preferences differ from those of the CHSs[1,2].

By using antisense transformation of *G. hybrida* with the *gchs2* cDNA, we obtained 14 plant lines that lacked *gchs2* expression partially or completely[7]. We next analysed methanol extracts from leaf, floral stem and corolla tissue of four transgenic lines, and from non-transgenic plants. This analysis showed that downregulation of *gchs2* correlates with the absence of a dominant substance found in control plants (Fig. 1a, b). In non-transgenic plants, the ontogenetic distribution of this substance correlates with the presence of *gchs2* messenger RNA (found in large amounts in all tissues except anthers), but not with the transcripts of the other CHS-related genes. A partial suppression of CHS genes takes place in the

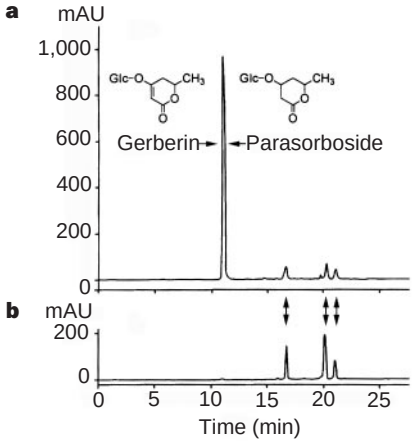

Figure 1 HPLC analysis of methanol extracts from leaves. **a**, Wild-type plant. **b**, *gchs2* antisense transformant, with no detectable *gchs2* expression. The major peak in **a** contains a mixture of gerberin and parasorboside. The peaks marked with arrows in **b** are hydroxycinnamic acid derivatives which are present at higher concentrations in the transgenic plants. A second independent transformant with no detectable *gchs2* mRNA also showed the pattern seen in **b**. Two more transformants with partial antisense effect (17% and 97% of wild-type *gchs2* mRNA was detected) showed a reduced gerberin/parasorboside peak (17% and 72% of the wild-type, respectively). Corolla samples from antisense plants showed the same pattern of change as leaves. The wavelength used for detection of the pyrone derivatives (254 nm) does not detect most flavonoids, but analyses at the appropriate wavelength indicate that their concentration is affected only sightly (<10% reduction) in *gchs2* antisense transformants. HPLC was done with an RP18 column, a linear gradient from 100% phosphoric acid (pH 2) to 100% methanol in 30 min, and a flow rate of 1 ml min^{-1}. mAu, absorption units $\times 10^{-3}$.

‖ Present address: The Lewis B. and Dorothy Cullman Program for Molecular Systematics Studies, The New York Botanical Garden, Bronx, New York 10458-5126, USA.